Chapter 3

The effects of absorption on the polarization from accretion disk atmospheres

3.1 Introduction

As discussed in chapter 1, Hubble Space Telescope spectropolarimetry data has revealed that in three radio quiet quasars, the polarization increases steeply with frequency in the ultraviolet (Impey et al. 1995; Koratkar et al. 1995). In all three objects, the polarization rise begins just blueward of the Lyman edge, strongly suggesting that the rise is associated with the physics of hydrogen. In the context of accretion disk models, these results are particularly disturbing as exactly the opposite behavior was predicted: the increased absorption opacity blueward of the edge should decrease the importance of electron scattering and reduce the polarization (LNP). What is more, in the case of PG 1630+377 the polarization rises to $\simeq 20$ percent, well *above* the maximum value expected from an optically thick, pure electron-scattering atmosphere and therefore apparently beyond the reach of a standard, optically thick accretion disk.

In this chapter, we propose that the resolution of the problem may be in the treatment of how absorption opacity affects the polarization. In their calculation of the standard disk, LNP simply assumed that absorption opacity reduced the Chandrasekhar polarization by a factor $q = \kappa_{es}/(\kappa_{es} + \kappa_{ab})$, where κ_{es} is the Thomson opacity and κ_{ab} is the absorption opacity, which we have also used

in our calculations of disk models in chapter 2. This factor was assumed to be vertically constant at each radius, determined by the temperature and density at the disk photosphere. This simple approach is technically incorrect and can in fact give qualitatively wrong answers. The degree of polarization is only proportional to q if $q \ll 1$, i.e. $\kappa_{es} \ll \kappa_{ab}$, so that the transfer equations can be solved perturbatively (e.g. Gnedin and Silant'ev 1978, Cheng et al. 1988). Even in this case, the function which q multiplies to give the degree of polarization is *not* in general the Chandrasekhar polarization, and can be much larger for steep thermal source functions or even rotated by 90° for flat thermal source functions. In an atmosphere with vertically constant q and with all photon sources at infinite depth (this includes the pure electron scattering atmosphere in the $q \to 1$ limit), the polarization in fact *increases* with increasing absorption opacity for q not too small (Loskutov and Sobolev 1979). In addition, the opacity κ_{ab} and therefore q are generally not independent of optical depth in the atmosphere, and should be integrated along with the polarized source function (cf. Loskutov and Sobolev 1981).

In realistic atmospheres, absorption opacity can enhance limb darkening and increase the polarization above the pure scattering value, provided the source function varies steeply with depth. This was demonstrated long ago in models of Mira variables by Harrington (1969). In addition, the standard Kurucz stellar atmospheres also tend to show this effect in the ultraviolet (Bochkarev, Karitskaya, and Sakhibullin 1985, hereafter BKS). Unfortunately, none of these authors ever published calculations of the polarization blueward of the Lyman edge. We demonstrate below that in a complete treatment of the radiative transfer through the atmosphere, absorption opacity can in fact increase the degree of polarization in this region of the spectrum, to values substantially larger than the pure electron scattering case. In section 3.2 we discuss the basic assumptions behind our treatment of the accretion disk atmosphere. Then in section 3.3 we present our results on the flux and polarization around the Lyman edge. In section 3.4 we discuss our conclusions. Two appendices, sections 3.5 and 3.6, discuss the grey atmosphere and complete linearization procedures we used to construct atmospheres.

As far as we are aware, the only other models to explain the observed polarization rises blueward of the Lyman edge is by Blandford and Lee (1997) who postulate resonance line scattering in an outflowing wind, and the Blandford and Phinney model of a Faraday screen with gaussian magnetic field, discussed in chapter 2.

3.2   The atmosphere calculation

We treat the local disk photosphere as an atmosphere with blackbody radiation emerging from below. As discussed in chapter 1, this may not be a good approximation, depending on the viscosity prescription, and future simulations should test this assumption. In the absence of external illumination (i.e. for the standard disk without, e.g., a corona), only two parameters determine the emergent spectrum and polarization from each zone: the local effective temperature T_{eff} and surface gravity g. We assume that g is constant with height in the atmosphere, which is a good approximation provided the atmosphere scale height is much smaller than the local disk thickness (which is rather insensitive to viscosity prescription, Sakimoto and Coroniti 1981), which we find to be true in our simulations.

We have written a code to calculate fully self-consistent models of non-LTE transfer of polarized radiation through pure hydrogen atmospheres. The code uses a Feautrier method combined with complete linearization (e.g. Mihalas and Mihalas 1984) to calculate all properties of the atmosphere. This includes the frequency, polarization, and angular distributions of the radiation field, as well as the temperature, density, pressure, and level populations determined self-consistently under the assumptions of hydrostatic, radiative[1], and statistical equilibrium. The polarization dependence of the scattering source function is included. In the absence of any absorption opacity, the code successfully reproduces the polarization results of Chandrasekhar (1960) and Phillips and Mészáros (1986).

Our model hydrogen atom consists of a user-specified number of explicit bound levels plus continuum. The negative hydrogen ion and molecular hydrogen are entirely neglected. The sources of absorption opacity included are free-free (modified to include photoionization from all the upper, non-explicit bound levels, and assumed to be in LTE, e.g. Hubeny 1988), and photoionization from the explicit bound levels. We assume the hydrogen atoms are unpolarized. All line opacities are neglected for the results presented here. The bound-free and free-free Gaunt factors g_{II} and g_{III} are taken to be unity, except for photoionization from the ground state where the exact absorption cross section is used. The only source of scattering opacity that we consider is Thomson scattering.

---

[1]In principle, substantial viscous dissipation might occur right near the disk photosphere so that radiative equilibrium will not be valid. However, given that we have no basic understanding of dissipation in disks, we neglect this possibility here.

The variation with frequency of the free-free Gaunt factor is gradual, and thus does not affect our conclusions near the Lyman edge.

We used a grid of 40 frequency points from 4.1×10^{13} Hz to 1.3×10^{17} Hz, chosen to resolve the Lyman edge region, distributed as follows. Ten points were logarithmically spaced redward of the Balmer edge, ten points were evenly spaced between the Balmer edge and the Lyman edge (at ν_0), ten points were evenly spaced between ν_0 and $2\nu_0$, and ten points were logarithmically spaced blueward of $2\nu_0$. Frequency quadratures were calculated according to Simpson's rule. The angular distribution of the radiation field in μ, the direction cosine of a ray with the vertical direction, was calculated on a grid defined by two separate n-point Gaussian quadratures in the range $-1 \le \mu \le 0$ and $0 \le \mu \le 1$. For the results presented in this paper, we used $n = 16$. We adopted an atmosphere depth grid at 40 fixed surface mass density values, spaced evenly in logarithm from 1.6×10^{-6} to 100 g cm^{-2}.

After calculating a series of individual atmospheres corresponding to each radial zone, we combine the results together to produce the disk spectrum. In the initial calculations presented here, we neglect entirely the relativistic transfer function on the spectrum and polarization, which will be presented in chapter 5.

3.3   Results

We have run the code with a range of values of T_{eff} and g appropriate for quasar accretion disk models. Redward of the Lyman edge, the polarization generally rises towards the blue. At the edge, the polarization drops due to the increase in absorption opacity, and then rises rapidly above the value for pure electron scattering as the bound-free opacity decreases. The polarization peaks at several hundred Ångstroms, and then falls towards the extreme ultraviolet. We find that there is an edge and rise in polarization even if there is none in total flux.

In chapter 2, we used the model of LNP which assumes that the polarization is given by qP_{ch}, where P_{ch} is the polarization of an electron scattering atmosphere. They chose q to be defined at $\tau^* = 2/3$, where $\tau^* = \kappa_{ab}/(\kappa_{ab} + \kappa_{es})^{1/2}$, since this is the average depth at which photons are created at a given wavelength. To facilitate comparison of our results with those of LNP, we have taken our atmosphere structure and calculated $q(\tau^* = 2/3)$ at all frequencies. The results are plotted in figure 3.1. Note that redward of the Lyman edge, our re-

sults agree rather well; however, blueward of the Lyman edge, the polarization from our atmospheres is significantly higher than that expected using LNP's approximation.

In figure 3.2, we show the variation of $q(\tau)$ and the source function with optical depth for various wavelengths for a $T_{eff} = 20,000$ K, $g = 130$ cm s^{-2} LTE atmosphere. At short wavelengths, the source function varies steeply with optical depth because in the Wien region the Planck function depends sensitively on the temperature. In this atmosphere, the maximum polarization is achieved at 456Å when the source function is very steep at $\tau = 1$ *and* the absorption opacity is not too strong relative to the electron scattering opacity ($q \simeq 1$). The physics here is in agreement qualitatively with the results of BKS. The large gradient in source function causes stronger limb darkening, so that for small μ, relatively more photons are seen due to scattering than due to emission, causing an increase in polarization. Figure 3.3 depicts this situation.

In addition, if q is too small at $\tau = 1$ (as at 912Å$-$, i.e. at a wavelength just short of the Lyman edge), then overall more photons emerge from the atmosphere without scattering, decreasing the polarization and in fact the limb darkening. If the source function at $\tau = 1$ is very flat (as at 13850Å), then limb darkening is weak and the scattered photons will mostly come from the side rather than below. This causes the polarization plane to be vertical, i.e p to become negative, for $\mu > 0.3$ at this wavelength. In Figure 3.4 we show the dependence of polarization on T_{eff}, and corresponding low values of g so that the atmosphere is nearly at the Eddington limit (including absorption opacity), for $\mu = 0.548$. The polarization for a pure electron scattering disk at the same viewing angle would be $\simeq 2$ percent. We easily obtain values larger than this blueward of the Lyman edge. In fact, in the lowest temperature atmosphere such large values are even obtained redward of the edge because of the longer wavelength Wien turnover in the Planck function. Note that all the polarizations approach the pure electron scattering value at zero wavelength, because in this limit the absorption opacity vanishes and the thermal source function is irrelevant. At very long wavelengths for this inclination angle, p is negative which has the potential of explaining the fact that the optical polarization is aligned with the radio axes in Seyfert 1's. This will depend however on the radial temperature gradient in the disk.

Figure 3.5 compares the results of a single temperature LTE atmosphere fit to the ultraviolet polarization data for the spectrum and polarization of PG1222+228 (Impey et al. 1995). We did not fit the flux since the observations
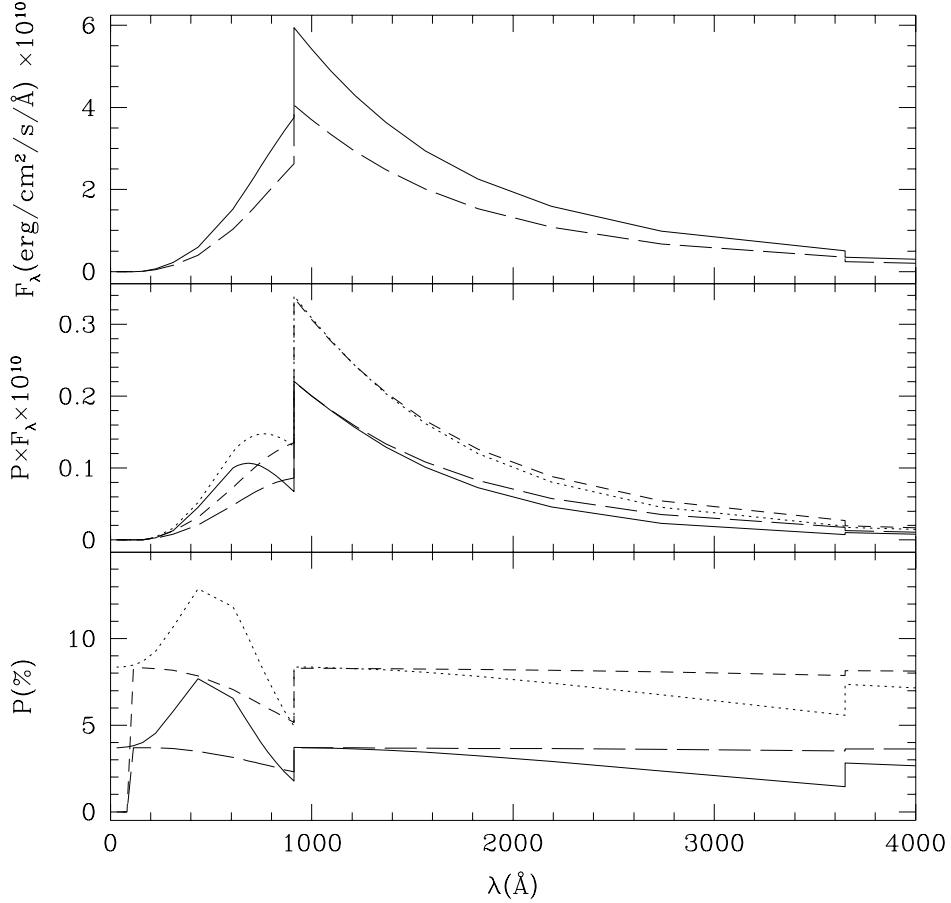
Figure 3.1: Comparison of our polarization calculation with the approximation used by LNP. The top panel shows the flux, the middle panel the polarized flux, and the bottom panel the percent polarization versus wavelength (the fluxes are multiplied by 10^{10} for legibility of the axis labels). The atmosphere has $T_{eff} = 20,000K$ and $g = 130$cm s^{-2}, in LTE. The dotted and solid curves are for $\mu = 0.069, 0.33$, respectively, and the dashed curves are LNP's approximation for the same μ's. The drop in polarization at small λ for LNP's approximation is due to the fact that at those frequencies, $\tau^* = 2/3$ is below the bottom of the atmosphere, which has a column density of 100 g cm^{-2} at the bottom.
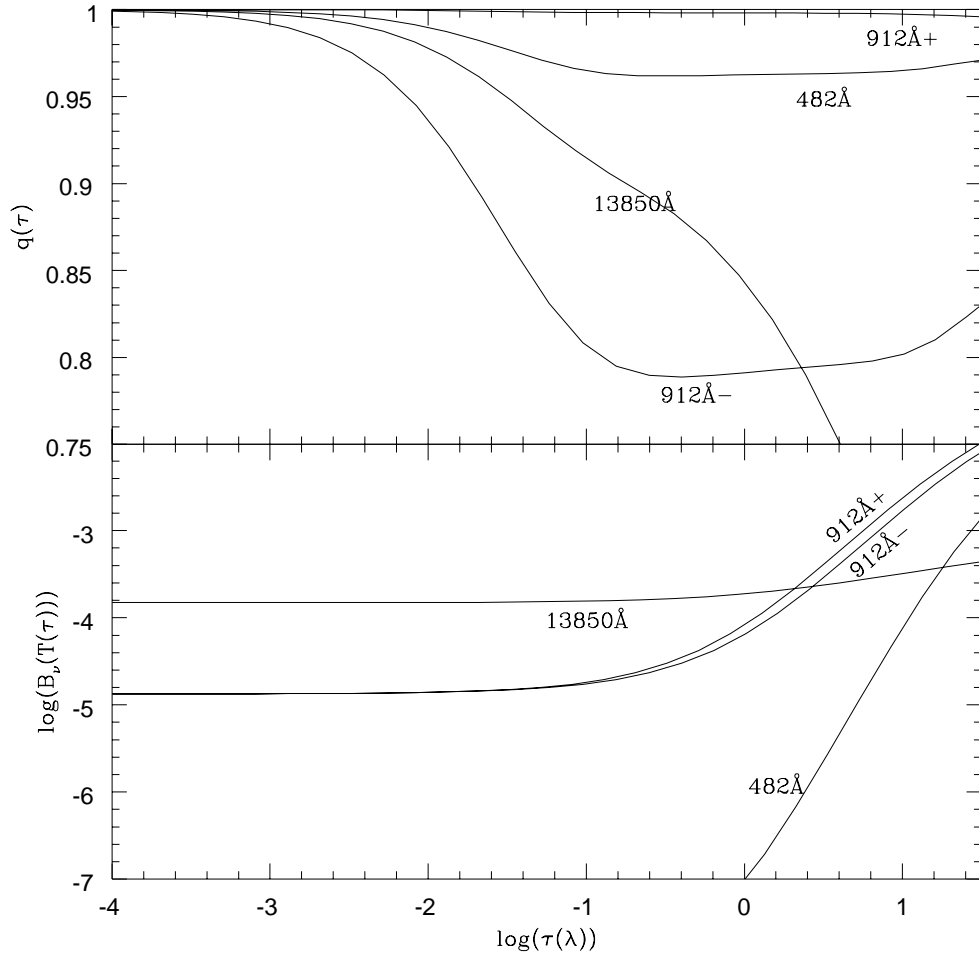
Figure 3.2: Variation of $q = \kappa_{es}/(\kappa_{es} + \kappa_{ab})$ and the thermal source function for various wavelengths for a $T_{eff} = 20,000$ K, $g = 130$ cm s^{-2} atmosphere.
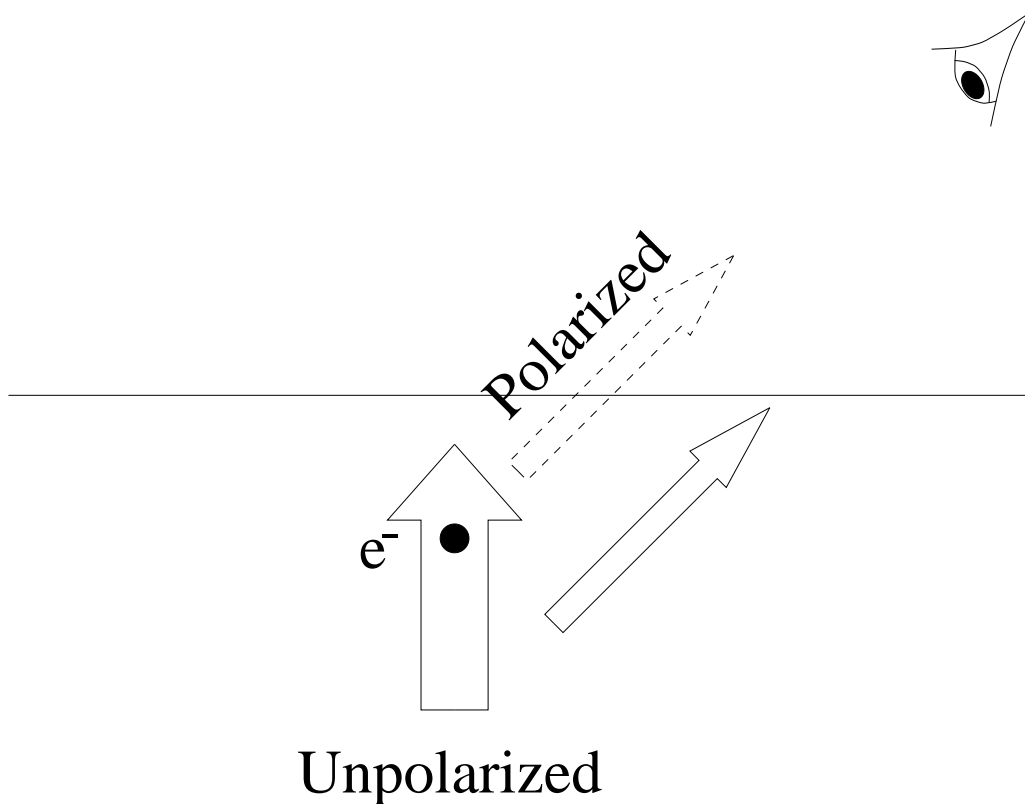
Figure 3.3: Illustration of the effect of limb darkening on the polarization emerging from an atmosphere. When modest absorption plus a steep thermal source function are present, there is enhanced limb darkening. The width of each arrow represents the strength of the radiation in that direction. The solid arrows represent the direct thermal emission, while the dashed arrow represents the scattered flux. The strong upward going flux leads to a strong scattered flux compared to the direct, unpolarized flux, leading to a strong polarization.
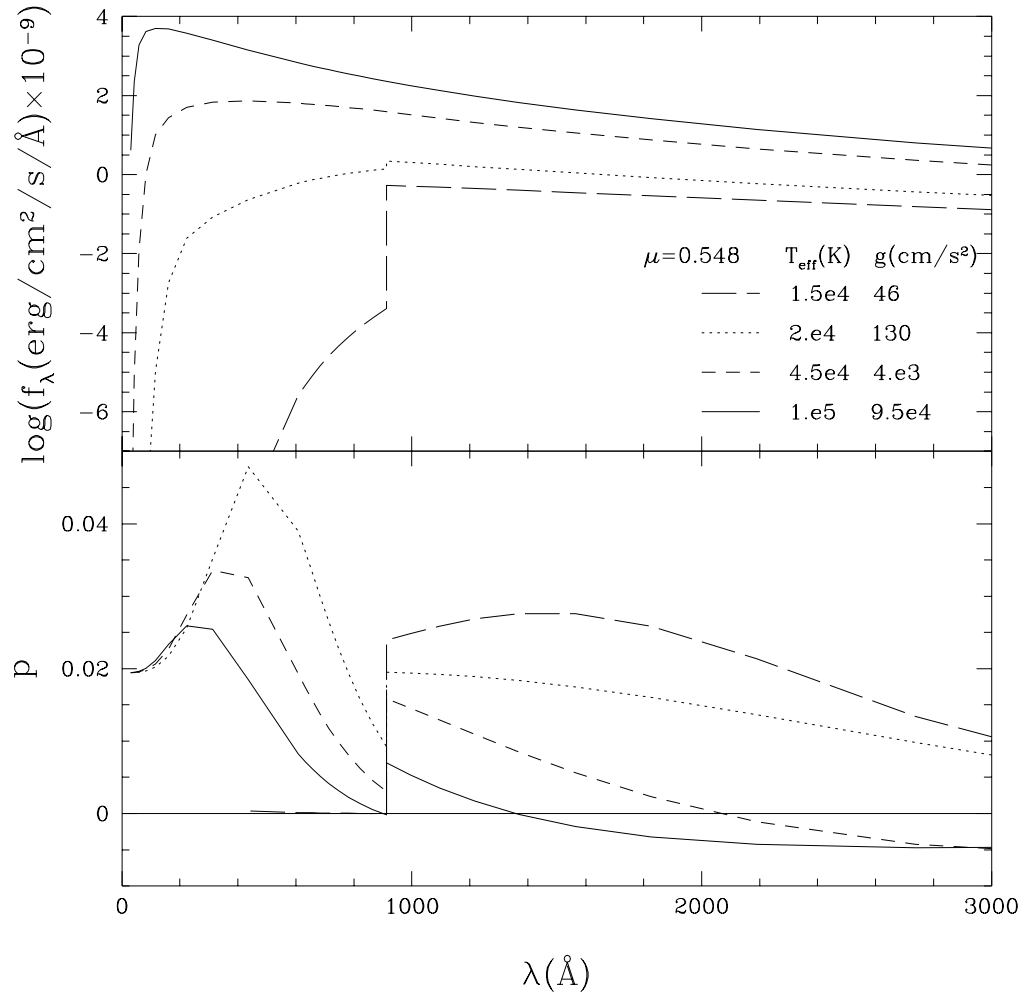
Figure 3.4: The total flux and polarization of the emerging radiation field as a function of wavelength for different effective temperatures and surface gravities, at $\mu = \cos i = 0.548$, where i is the inclination angle of the line of sight to the observer with respect to the normal of the plane of the atmosphere.
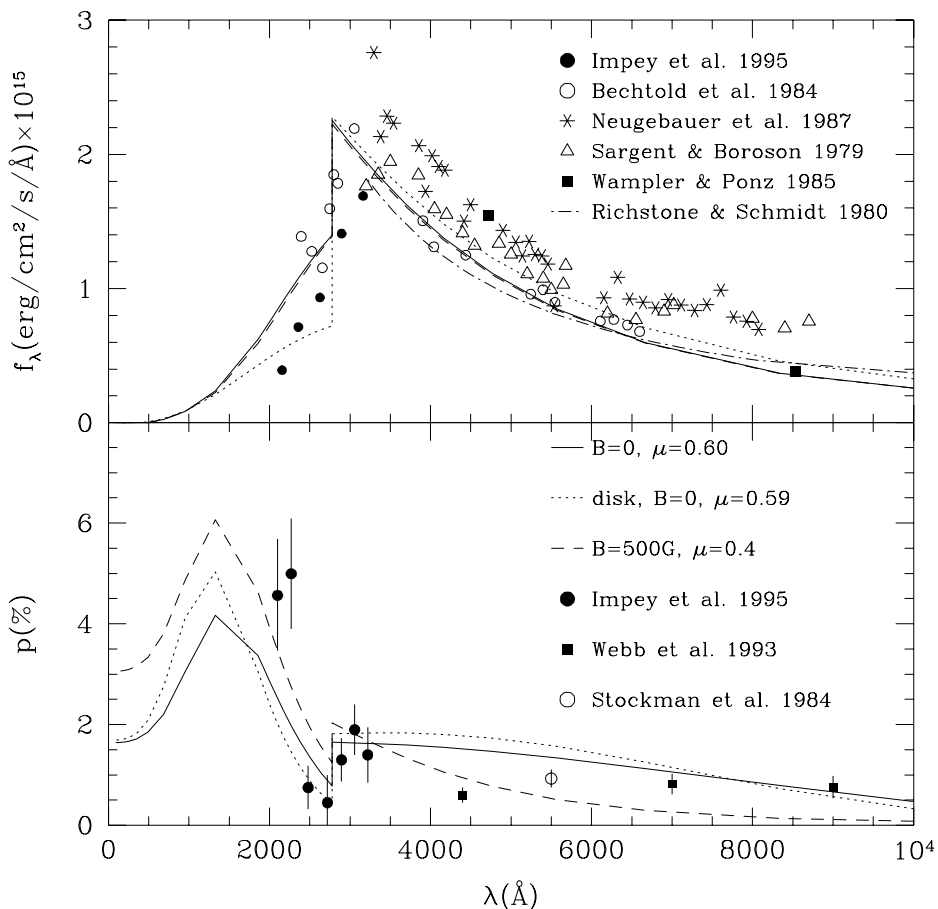
Figure 3.5: The total flux and polarization versus observed wavelength (z=2.047) of PG1222+228. Solid curves show the best least-squares fit to the UV polarization data (the seven shortest wavelength points) for a $T_{eff} = 20,000$ K, $g = 130$ cm s^{-2} atmosphere model, yielding $\mu = 0.59$, $\chi^2 = 15$. Also shown are curves for the multi-temperature disk model described in the text, with best fit $\mu = 0.60$, $\chi^2 = 18$. Finally, a case illustrating the effects of Faraday rotation in a single-temperature atmosphere model is shown, with $\mu = 0.4$, $B = 500$ G, $T_{eff} = 20,000$ K, $g = 130$ cm s^{-2}, and $\chi^2 = 23$. The theoretical fluxes shown in the upper half of the figure were scaled by an arbitrary constant for each model to roughly agree with the (nonsimultaneous) flux data.

are non-simultaneous, and thus it is uncertain whether the quasar has varied between observations, so instead we scaled our calculated flux by an arbitrary constant to compare to the observations. The steepest rise in polarization blueward of the Lyman edge occurs for $T_{eff} \simeq 20,000$ K, so we used this model atmosphere to make a best fit to the UV polarimetry data from (Impey et al. 1995), minimizing χ^2 by varying μ. Using this prescription, we also performed a least-squares fit by varying μ and B, which is also shown in Figure 3.5. The model provides a good qualitative fit to both the observed spectrum and polarization, particularly given that we did not attempt to fit the spectral energy distribution of total flux. This suggests to us that this physics may indeed be responsible for the observations. However, there are clearly quantitative differences between the fit and the data. Blueward of the edge, the first two polarization data points are both above the fit while the second two points are below, indicating that our model does not produce as fast a rise as observed. The position angle of polarization in this simple model is parallel to the disk plane. Radio axes have not been observed in these particular sources, so we do not yet know the orientation of the putative disk plane.

We have also calculated disk spectra by summing LTE atmospheres over radius, with g and T_{eff} calculated from a standard one-zone accretion disk model (Novikov and Thorne 1973), which doesn't include bound-free opacity, including the corrections of Page and Thorne (1974), Eardley and Lightman (1975), and Riffert and Herold (1995). We increased g by 20% to take into account the effects of increased opacity due to bound-free absorption on the vertical height of the disk. We took the emitting area of each annulus to be given by the Euclidean expression and neglected the relativistic transfer function on the spectrum and polarization, which will be taken into account in chapter 5. The disk model is taken from Webb et al. (1993): $M = 5.3 \times 10^9$ M$_\odot$, $L = 0.092 L_{Edd}$, $\alpha = 0.1$, and $a = 0$. The disk extends from the inner edge, with $T_{eff} = 24,000$ K, $g = 300$ cm s^{-2}, to $r = 50 r_g$, where $T_{eff} = 11,000$ K, $g = 14$ cm s^{-2}. We did not go to larger radii since our code had difficulty converging for low T_{eff}. The best fit to the polarization is shown in Figure 3.5. The polarization doesn't fit as well as for the 20,000K atmosphere because the maximum temperature in this disk is slightly higher (maximum $T = 25,500$ K at $r = 9.5 r_g$). The jump in flux across the Lyman edge is much stronger for the disk we calculated than for the 20,000K atmosphere because of the contribution of the lower temperature regions of the disk which are less ionized, making a stronger edge. This is a well-known problem with accretion disk models, as discussed in chapter 1.

Faraday rotation by a photospheric magnetic field could in principle steepen the rise in polarization because longer wavelengths will be more depolarized, as shown in chapter 2 . We therefore calculated models including a vertical magnetic field as discussed in chapter 4. Figure 3 shows a case with a 500 G magnetic field in the $T_{eff} = 20,000$ K, $g = 130$ cm s^{-2} atmosphere. This model actually gives a poorer fit to the ultraviolet polarization data, but illustrates how photospheric magnetic fields may affect the models.

The flux and polarization near the Lyman edge are very sensitive to the exact value of g, so it will be important in future models to include the dependence of gravity on height in the calculation (Kříž and Hubeny 1986) rather than using the value of g from a single zone model. We are currently implementing this in our code. We have also tried fitting the data of PG1338+416 and PG 1630+377 (Koratkar et al. 1995), but the results are much less satisfactory since we cannot reproduce the quick rise in polarization with frequency and the data has no drop in polarization right at the Lyman edge as our model does. If we put an arbitrarily steep source function in the atmosphere, then we can reproduce the steep rise. We do not know a physical reason for why such a steep source function might occur.

Finally, we have calculated some models with the $n = 1$ and 2 levels of hydrogen in non-LTE. In principle non-LTE effects could change the polarization because the gradient of the thermal source function is no longer that of the Planck function. However, we have found that the polarization rise is similar, although the Lyman edge can be in emission (for low g) or absorption in total flux. Figure 3.6 shows a comparison of the LTE atmosphere with a non-LTE atmosphere for the same parameters; the emission edge is quite strong in the non-LTE case (the flux is on a log scale), which has important implications for modelling accretion disks. If a Lyman emission edge cannot be comptonized or blurred by relativistic effects, then this will severely constrain accretion disk models. Models with external illumination (Sincell and Krolik 1997) and more sophisticated non-LTE models (Hubeny and Hubeny 1997) frequently show emission edges. This also agrees with the results of (Störzer, Hauschildt, and Allard 1994), who find that non-LTE effects tend to reduce the absorption edge or even drive it into emission. The Balmer edge is weaker in the non-LTE atmosphere than in the LTE, which means that the 4000 Å break may not be caused by Balmer continuum absorption.
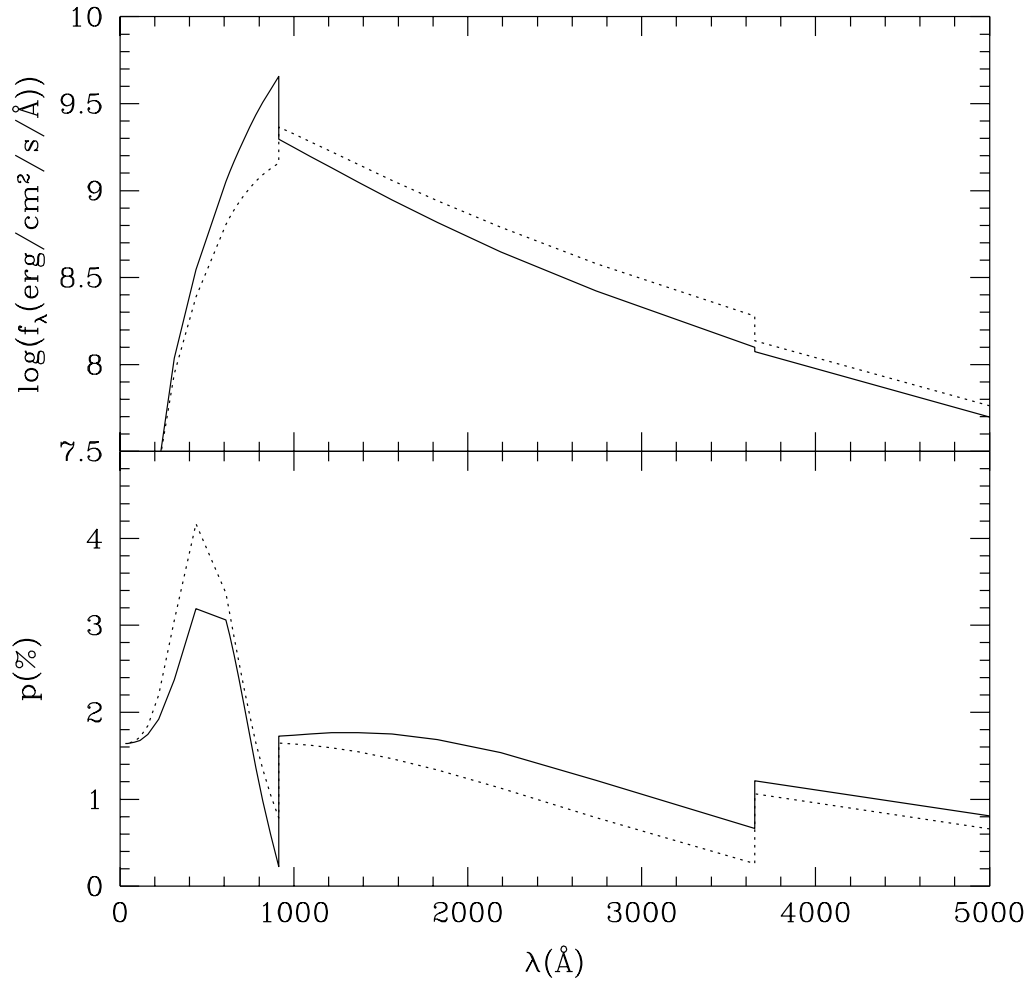
Figure 3.6: Comparison of a non-LTE atmosphere (solid line) with an LTE (dashed line) for $\mu = 0.6$, $T_{eff} = 20,000$K, $g = 130$cms^{-2}, two levels of hydrogen.

3.4 Conclusions

If the rise in polarization blueward of the Lyman edge in PG1222+228 arises from an optically thick atmosphere with hydrogen bound-free opacity, as suggested by the fit from our spectrum, then we predict that the polarization will continue to rise towards the ultraviolet, and will start to drop at several hundred Ångstroms in the quasar rest frame, although this might be affected by additional sources of opacity from elements heavier than hydrogen. This could have been tested by further observations with the Hubble Space Telescope with the G130H grating on the Faint Object Spectrograph; however, this instrument is now removed. Also, the spectrum is severely absorbed at shorter wavelengths, which will make these observations difficult.

More generally, we expect that higher temperature atmospheres will not show such steep rises in polarization in this wavelength region because the steepness of the source function relies on the sensitive temperature dependence of the Wien limit of the Planck function. We therefore predict that quasars which have continuum spectra indicating low temperature atmospheres are the best ones to look for steep rises in polarization. For the same reason, we do not expect dramatic rises in polarization to be associated with longer wavelength atomic edges, unless the atmosphere is much cooler. Note that both of these predictions depend on the actual vertical temperature gradient not being very steep itself at unit optical depth. If for some reason it is, then high polarization could again be produced.

Lastly, we predict that the polarization blueward of the Lyman edge is perpendicular to the symmetry axis in these objects. Otherwise, the plane-parallel geometry is wrong, but the wavelength dependence may still arise from absorption effects. We would encourage radio observations to look for extended emission to test this prediction.

The results presented here are just preliminary steps towards calculating self-consistent accretion disk models. While we believe these results to be suggestive, we have not yet achieved a good quantitative fit to the flux and polarization data. It is clear that if stellar atmosphere physics is responsible for the observed rises in polarization, then this problem is intimately related to the Lyman edge problem in quasars (Antonucci, Kinney, and Ford 1989; Koratkar, Kinney, and Bohlin 1992b). It is possible that the Lyman edge problem will have to be solved by examining more sophisticated models, including the height dependence of g, relativistic effects, further sources of opacity, or other possibilities than simple

thin disks, such as disks which are not completely optically thick and disks with illumination from a corona or other external source. In an optically thin disk, the fact that the rise starts somewhat blueward of the Lyman edge might be caused by the isotropic emission of Lyman continuum photons which are produced immediately blueward of the edge from recombinations in a cool atmosphere. Shorter wavelengths suffer true absorption with little reemission, and can therefore be more anisotropic and polarized. On the other hand, reducing the optical depth of a disk will make it hotter at fixed effective temperature. Two-phase models (e.g. Haardt and Maraschi 1991; Svensson and Zdziarski 1994) might produce steep rises in polarization by ensuring a relatively cool inner disk. In addition, external illumination by a corona of large scale height or ion torus could heat the outer parts of the disk, smoothing the radial temperature gradient. As discussed in section 3.3, this would improve our fits to the observed polarization. Flatter temperature gradients would also provide better agreement with the observed optical/UV spectral energy distributions, which typically have spectral indices α ($F_\nu \propto \nu^\alpha$) in the range -0.3 to -0.2 rather than $+1/3$ as predicted by the standard disk (e.g. Barvainis 1993,Webster et al. 1995). High levels of polarization might also be produced from coronal UV emission which is scattered off the cold disk (cf. Matt, Fabian, and Ross 1993 who calculated this effect in the X-rays). Indeed, reprocessing of coronal emission is one way that disks can overcome the problem of near simultaneous UV/optical variability observed in Seyferts (e.g. Krolik et al. 1991).

3.5   Appendix A: grey atmosphere

Since complete linearization is essentially a multidimensional Newton's method, to converge on an atmosphere requires a starting approximation. We calculated a grey atmosphere by the following procedure:

(1) We initially assume the hydrogen is fully ionized and thus the opacity is given by the electron scattering opacity. We first assumed the temperature distribution of a grey atmosphere using the Eddington approximation:

$$T = \left[\frac{3}{4}T_{eff}^4\left(\tau + \frac{2}{3}\right)\right]^{\frac{1}{4}}. \tag{3.1}$$

(2) We calculate the effective gravity throughout the atmosphere: $g_{eff} = g - \sigma_b T_{eff}^4 \sigma_{th} c^{-1} m_p^{-1}$, where σ_b is Boltzman's constant, σ_{th} is the electron scattering

cross section, m_p is the proton mass.

(3) We then calculate the gas pressure, p_g throughout the atmosphere by integrating the hydrostatic equilibrium equation: $p_g = \int_0^m g_{eff} dm$, where m is the mass column depth from the top of the atmosphere in g//cm^2. From this we calculate the total number density of particles: $n_{tot} = p_g k^{-1} T^{-1}$.

(4) Next, we calculate the number density of electrons, protons, and hydrogen in the excited levels, assuming LTE:

$$n_e = n_{tot}/(1 + \sqrt{1 + n_{tot} \Phi_{sum}}) \tag{3.2}$$

$$\Phi_{sum} = \sum_{i=1}^{n_l} \Phi_i(T) \tag{3.3}$$

$$\Phi_i(T) = i^2 \left(\frac{h^2}{2\pi m_e k T} \right)^{\frac{3}{2}} e^{\frac{h\nu_0}{kTi^2}} \tag{3.4}$$

$$n_{HI,i} = n_{HII} n_e \Phi_i(T) \tag{3.5}$$

$$n_{HII} = n_e \tag{3.6}$$

$$\tag{3.7}$$

where n_e is the electron number density, n_l is the number of hydrogen bound levels included, $\Phi_i(T)$ is the Saha-Boltzmann factor, m_e is the electron mass, $h\nu_0$ is one Rydberg, $n_{HI,i}$ is the number density of the ith level of hydrogen, and n_{HII} is the proton number density.

(5) Using the current approximation for the atmosphere structure, we calculate the Rosseland mean opacity at each depth. The opacities we use are the exact ionization opacity for the ground state of hydrogen, and the following approximation for the higher levels of hydrogen: $\alpha_{i,II} = 2.815 \times 10^{29} \nu^{-3} i^{-5} \text{cm}^2$ for $\nu > \nu_0 i^{-2}$.

(6) We then recompute the Rosseland optical depth as a function of column depth: $\tau = \int_0^m \chi_R \rho^{-1} dm$.

(7) We recompute the temperature as in step (1). We recompute the effective gravity, but now using the Rosseland opacity: $g_{eff} = g - \sigma_b T_{eff}^4 \chi_R c^{-1} \rho^{-1}$.

(8) We repeat steps (3)-(7) 20 times, which is sufficient to reach convergence.

3.6   Appendix B: complete linearization

The radiative transfer calculations were described in more detail in chapter 2. The Feautrier method (Feautrier 1964) is used to solve the equations of transfer,

which is described in detail in Mihalas and Mihalas (1984, section 83). Mihalas and Mihalas (1984, section 88) also describe the complete linearization method, in which each variable is treated separately from the others. The radiative transfer equations, hydrostatic equilibrium equation, radiative equilibrium equation, number and charge conservation equations, and equations of statistical equilibrium are all linearized. These equations and their method of solution are described in detail in Mihalas and Mihalas (1984), so we will only sketch the outline here. The method of solution goes as follows:

(1) The grey atmosphere is used a starting approximation, or an input atmosphere from previous calculations is used.

(2) The polarized radiation field is solved exactly for the current atmosphere structure at all depth, frequency, and angle points using the Feautrier method. From this, the mean fluxes, Eddington factors, and geometrical factors for the upper boundary condition are computed (summing over polarizations).

(3) The linearized atmosphere equations are inverted to solve for the changes in all variables, again using the Feautrier method to invert the matrices.

(4) The statistical equilibrium equations are solved for the number densities of each ionization state, holding the radiation field and temperature fixed.

(5) Steps (2)-(4) are repeated until the average change in all of the variables is less than 0.1%.

For LTE atmospheres, we used the grey atmosphere as a starting approximation. We begin by using only two angle quadrature points (in each quadrant) in step (2), and once an atmosphere solution is found, we iterate to convergence using 16 angle quadrature points. For non-LTE atmospheres, we use the LTE atmosphere as an input, again using 2 and then 16 angle points.

For the non-LTE atmospheres, we used collisional rates from Mihalas (1967, appendix II). In calculating the statistical equilibrium equations, we ignore the bound-bound transitions.